Nanoscale

Accepted Manuscript

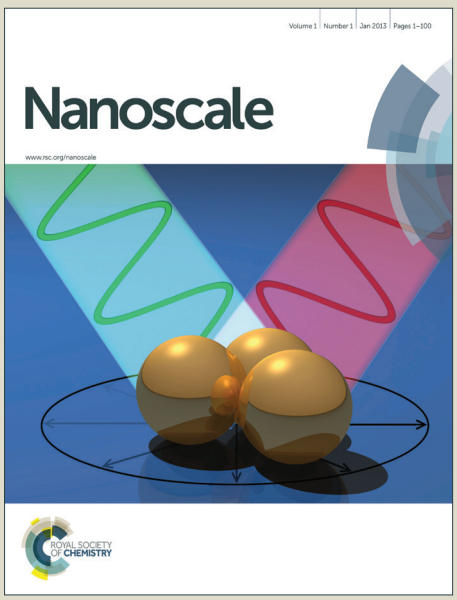

ROYAL SOCIETY OF CHEMISTRY

www.rsc.org/nanoscale

Journal Name

RSCPublishing

ARTICLE

Cite this: DOI: 10.1039/x0xx00000x

Direct imaging of the magnetic polarity and reversal mechanism in individual $Fe_{3-x}O_4$ nanoparticles

Moya Carlos,[*‡a] Iglesias-Freire Óscar,[‡b,c] Pérez Nicolás,[a] Batlle Xavier,[a] Labarta Amilcar [a] and Asenjo Agustina[b]

Received ooth January 2012,
Accepted ooth January 2012

DOI: 10.1039/x0xx00000x

www.rsc.org/

This work reports on the experimental characterization of the magnetic domain configurations in cubic, isolated $Fe_{3-x}O_4$ nanoparticles with a lateral size of 25-30 nm. The magnetic polarity at remanence of single domain ferrimagnetic $Fe_{3-x}O_4$ nanoparticles deposited onto a carbon-silicon wafer is observed by magnetic force microscopy. The orientations of those domains provide a direct observation of the magneto-crystalline easy axes in each individual nanoparticle. Furthermore, the change in the domain orientation with an external magnetic field gives evidence of a particle magnetization reversal mediated by a coherent rotation process that is also theoretically predicted by micromagnetic calculations.

Introduction

Magnetic nanoparticles (NPs) have been actively researched in the last decades due to their applications in technology – such as magnetic recording,[1] catalysis[2] or environmental remediation[3] – and in biomedicine[4] – including biomolecule detection,[5] magnetic hyperthermia[6] or targeted drug delivery.[7] In particular, magnetite $Fe_{3-x}O_4$ NPs are one of the most commonly studied systems because of their ease to be produced and functionalized by chemical routes,[8] low toxicity and magnetic properties.[9] In addition, they are excellent model systems to study finite-size effects, yielding insight into new phenomena and enhanced properties of nanomaterials with respect to their bulk counterparts.[10] Currently, the study of the composition and crystallinity of individual NPs on the sub-nanometer scale can be performed by electron microscopy techniques, as previously reported.[11] Moreover, the magnetic and the electronic properties of single NPs can be addressed by combining photoemission electron microscopy (PEEM) with synchrotron-based, polarization-dependent X-ray absorption spectroscopy (XAS).[12]

Another remarkable technique that allows the direct imaging of magnetic nanostructures is magnetic force microscopy (MFM),[13,14] a widespread technique that yields information about the distribution of magnetic charges within the surface region of ferrimagnetic samples. Its main advantages consist of a relatively high spatial resolution – allowing local measurements well below the microscopic scale – and versatility – enabling the possibility to apply external magnetic fields.[15] The capability of resolving small nanostructures, such as single nanoparticles, is limited by the finite radius of the tip apex, as well as by the tip-sample distance at which the magnetostatic interactions become dominant (typically 15-50 nm). The radius of the MFM tip can be decreased by using thinner magnetic coatings but the latter results in a lower magnetostatic coupling with the sample. Therefore, a balance must be met between resolution and sensitivity when aiming at characterizing magnetic nanostructures.[16] Although partially successful attempts to characterize individual magnetic NPs have been made;[17-26] the unambiguous correlation of the magnetic domain orientation to the crystalline structure is yet to be achieved. Within this framework, we present direct experimental observations of the magnetic domain configuration and magnetization reversal mechanism of individual $Fe_{3-x}O_4$ NPs. In addition, experimental analysis is further supported by micromagnetic calculations.

Experimental details

Samples were synthesized by high-temperature decomposition of Fe(III)–acetylacetonate in organic solvent with decanoic acid as capping ligand, as reported elsewhere.[8] Particle size distribution was analyzed by measuring around 1500 particles and the resultant histogram was fitted to a log-normal distribution function. Nanocrystals were found to be cubic in shape (see Figure 1.a and S1, Supporting Information), with a mean diameter of 27.2 nm and a standard deviation of 16.5 nm (see Figure 1c). Figure 1d shows iron oxide NPs to possess high crystal quality with an inverse spinel structure and an average particle diameter D_{XRD} = 27.0 ± 1.5 nm.

The saturation magnetization M_S was obtained by extrapolation of the high-field region of the magnetization curves *M(H)* to zero field, assuming that the high-field behavior is of the type $M_S+\chi H$, where χ is a residual high-field susceptibility.[27,28] M_S values were normalized to the magnetic content by subtracting the organic fraction to the sample mass.

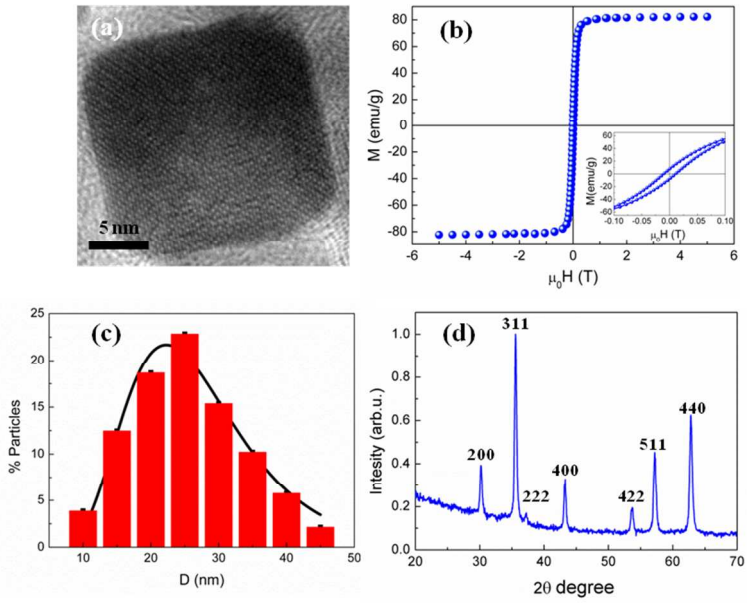

Figure 1. Structural and magnetic characterization. (a) High resolution TEM image of a single $Fe_{3-x}O_4$ nanoparticle. (b) Hysteresis loops of 27 nm $Fe_{3-x}O_4$ NPs at 300 K and detail of the low field region (inset to figure 1.b). (c) Particle size distribution obtained by TEM. The solid line corresponds to the fitting of the histogram to a log-normal distribution function. (d) X-ray diffraction pattern together with the indexation of the Bragg peaks to an inverse spinel structure.

The saturation magnetization obtained from the hysteresis loop at room temperature (RT) (M_S = 80.9 ± 0.2 emu/g) was just slightly smaller than the bulk value,[29] indicating an almost perfect ferrimagnetic order throughout the whole NP, as shown in Figure 1a and previously reported in samples with very high crystal quality synthesized by the thermal decomposition method.[27,28] The squareness of the hysteresis loop and the existence of a finite value of the coercive field at RT ($\mu_0 \cdot H_c$ = 10.7 ± 2.0 mT) are associated with the blocking of the particle magnetization in a non-superparamagnetic state (see Figure 1b). In such highly crystalline samples, well defined magneto-crystalline easy axes are expected to favor spins to point along the [111] directions, as has been demonstrated in macroscopic $Fe_{3-x}O_4$ crystals.[30] However, one should keep in mind that the magnetization data result from averaging over an enormous number of NPs – many of them with different orientations and grouped into clusters – in such a way that no direct evidence can be provided for the behavior occurring in isolated NPs. For that purpose, extracting local information about the magnetic properties of single particles becomes necessary.

Results and discussion

Figure 2 shows the topography and corresponding MFM images of four isolated $Fe_{3-x}O_4$ NPs, measured at remanence after in-plane saturation along the horizontal direction of the images. It is worth noting that, in contrast to the high accuracy yielded by AFM-based techniques in measuring vertical distances, lateral dimensions of protruding nanostructures are unavoidably overestimated due to the convolution of tip-sample interactions over the tip apex volume. Furthermore, sharp corners are considerably smoothed, as the dimensions of NPs are comparable to the tip apex radius. As a consequence, NPs shown in Figure 2 appear to be 2-3 wider than their real size and their cubic geometry is smeared out so that they appear as rather semi-spherical objects [31] (upper row in Figure 2). On the contrary, vertical distances get rid of the convolution effect and yield heights (Figure 2e) in outstanding agreement with the size histogram shown in Figure 1c.

The MFM images in Figure 2 show individual NPs at remanence to be single domain with well defined magnetic polarity, as expected for magnetite NPs of about 30 nm with high crystallinity. Furthermore, KPFM/MFM experiments were performed to discard electrostatic interactions and special attention was paid to the tip selection in order to get tip-particle interaction energy less than the anisotropy energy of a single particle so that the magnetization polarity remained unchanged while the image raster was completed. MFM images showing particles with distinct orientations of the magnetic polarity also rule out eventual influence of the stray field of the tip in the magnetic state of the particles or overlapping[32,33] of electrostatic interactions.[34,35]

Some misorientation of the magnetic polarity – expected from the rather stochastic processes governing the drying step– exists among NPs when comparing the relative orientation of the bright-dark regions in the MFM images of Figure 2. Interestingly enough, although two neighboring NPs seem to be present in the AFM image of Figure 2c, only one of them gives rise to contrast in the corresponding MFM map. This suggests the existence of organic residues from the synthesis process,

which might be misinterpreted as being $Fe_{3-x}O_4$ NPs in topographic images.

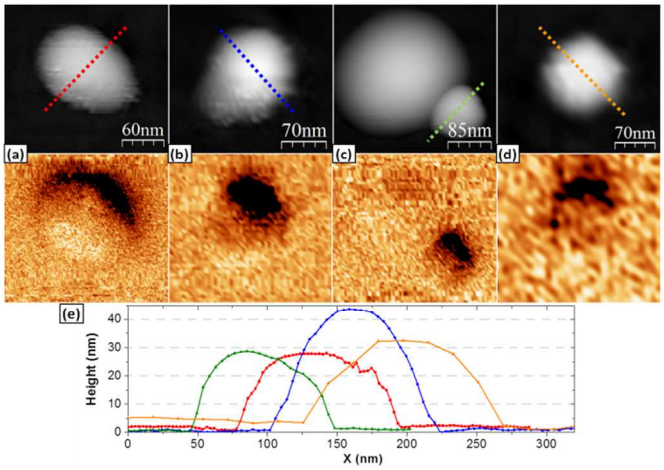

Figure 2. The remnant state. (a)–(d) Topographic AFM (top row) and corresponding MFM images (bottom row) of four different $Fe_{3-x}O_4$ NPs measured at remanence after in-plane magnetic saturation along the horizontal direction of the images. (e) Height profiles of those NPs in (a)-(d). Colored profiles in (e) correspond to the respective dashed lines depicted in the (a)-(d) AFM images.

The influence that an external field has over such domain configurations is described in Figure 3. Note that the area shown in Figure 3c corresponds to the zoomed NP in Figure 2c. If these $Fe_{3-x}O_4$ NPs were isotropic, the applied magnetic field would determine a preferential direction in terms of the energetic balance, so that, for field values large enough for spins to overcome eventual pinning potentials, domain polarizations would appear aligned with the external field in the MFM images. However, this is not the case in Figure 3, where the dipolar contrast clearly reflects the existence of other preferential directions for spins to point along. We attribute this to the magneto-crystalline easy axes along the [111] directions of the cubic NPs.

Particularly relevant from these results becomes the fact that the orientations of the particle domains change when reversing the external field, in such a way that it is not a simple reversal of the dipolar polarity. This can be readily seen when comparing the MFM images shown in the left and right columns of Figure 3, corresponding to magnetic field values larger than the coercive field of the NPs (at RT) with opposite directions. In each NP, the domain polarization changes from an orientation roughly inclined towards the right (↗ for positive values of the field) to another one inclined towards the left (↖ for negative fields), as the magnetic field is reversed. Thus, particle spin configuration accommodates to the magneto-crystalline easy axis that is closest to the direction of the external field. The similarity between the spin configurations observed in different NPs of the sample can be explained by the previous magnetic history followed by the system, in which magnetic fields close to the saturation field were applied. Most pronounced differences between the magnetic configurations of the NPs would be expected if the sample were in the virgin state.

Besides revealing the polarity and orientation of the particle domains, these MFM images yield additional information. The recorded switch in the spin orientation from one easy axis (for positive fields) to another one (for negative fields) is an experimental fingerprint of the reversal process being carried out by a coherent rotation mechanism. In order to support this hypothesis, some numerical calculations were performed by means of the OOMMF code [37] to simulate the magnetization distribution in cubic $Fe_{3-x}O_4$ NPs. The *3D Oxsii* mode was used with the following parameters: saturation magnetization, M_S = 4.66 kA/m, was obtained from the hysteresis loop (see Figure 1b); exchange stiffness constant for magnetite[38], $A = 13.2 \cdot 10^{-12}$ J/m; magneto-crystalline anisotropy constant for bulk magnetite[29], $k_1 = 12$ kJ/m^3 and a cubic cell size of (2x2x2) nm^3.

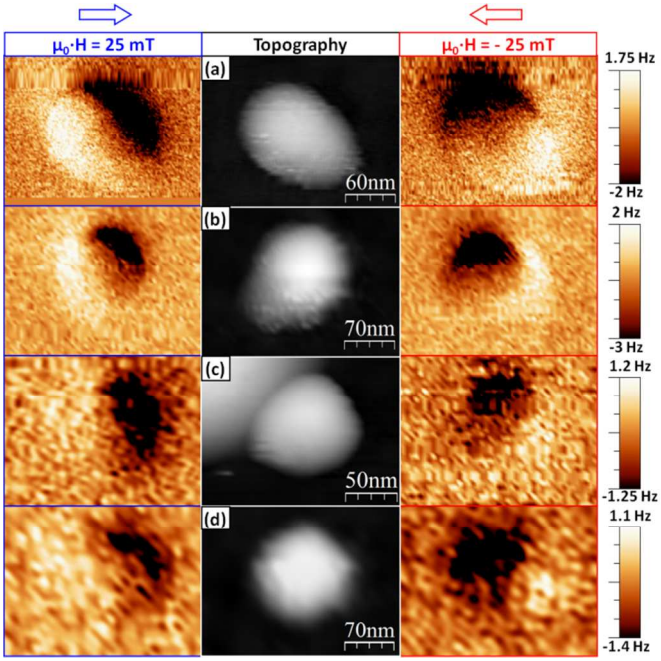

Figure 3. The domain polarity. Topographic (center) and MFM images (left & right) of the same NPs in figure 2(a)-(d), in the presence of in-plane magnetic fields with opposite directions (see blue and red arrows on top of the figure).

The simulated hysteresis loop of a single NP is displayed in Figure 4. This curve describes the reversal of the particle magnetization for the case of an in-plane field applied along the [100] direction (horizontal direction), similarly to the experimental situation. In the remnant state ($\mu_0 \cdot H = 0$), the NP is predicted to present a single domain configuration with its spins mainly aligned along the [111] axis. This causes the ratio of the remnant magnetization to the saturation magnetization to

be 0.58. The simulation predicts the reversal mechanism to follow a coherent rotation of the spins, as is displayed in Figure 4b, with a coercive field of $\mu_0 \cdot H_C$ = 26 mT. Since the dimensions of these NPs are rather small, it would be energetically costly in terms of the exchange energy to generate any kind of domain wall to carry out the reversal process. Thus, the NPs behave as a macrospin, tending to accommodate anytime to the closest crystalline easy axis, giving rise to the change of orientations shown in Figures 4a and 4c as the magnetic field reverses its polarity. So, as the micromagnetic simulations suggest, the switching between easy axes during the magnetization reversal process observed in the MFM images (see Figure 3) can be associated with a coherent rotation mechanism rather than with nucleation and propagation of domain walls.

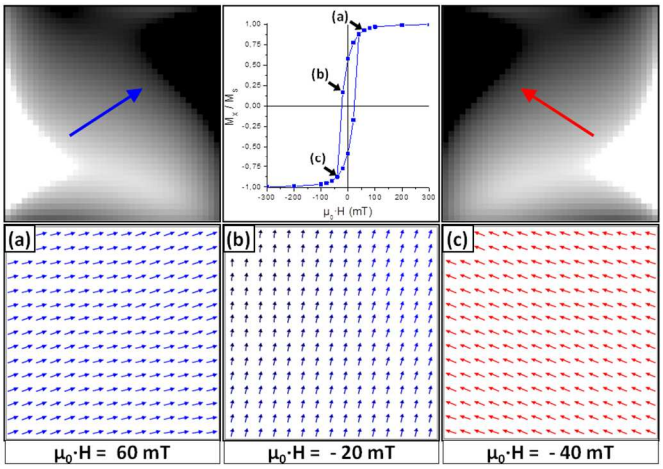

Figure 4. Micromagnetic simulations. (Upper center) OOMMF simulated hysteresis loop for an individual *NP* with an in-plane field applied along the [100] direction (horizontal direction). Bottom (a), (b) and (c) images: Distribution of the magnetization for the three situations highlighted by black arrows in the previous hysteresis loop. The upper left and upper right images display the simulated MFM contrast for the configurations presented below in the bottom (a) and (c) images, respectively.

Experimental Section

Samples for transmission electron microscopy (*MT80-Hitachi TEM*) analysis were prepared by drying at room temperature (RT) one drop of a dilute suspension of NPs deposited onto a carbon-coated copper grid. In order to get a deeper insight into the crystal quality and stoichiometry of individual NPs, high resolution TEM images (HR-TEM) were obtained with a *JEOL-2100F* microscope. The organic fraction of the samples was evaluated by thermogravimetric analysis (TGA) using a *TGA-SDTA 851e/SF/1100* (*Mettler Toledo*) set-up, at a heating rate of 10 K/min in nitrogen atmosphere from room temperature up to 1073 K (see Figure S2, Supporting Information). Hysteresis loops of powder sample of NPs were measured with a *Quantum Design* SQUID magnetometer under a maximum applied magnetic field of ± 5 T at 5 and 300 K. Samples for AFM-MFM observations were prepared by placing one drop of a dilute suspension of NPs onto a carbon-silicon wafer and drying it in an oven at 348 K for 1 hour in order to ensure all solvent traces were completely removed. We prepared several samples by varying the particle concentration, deposition conditions and the particle size in order to find regions where we were able to identify by AFM imaging isolated particles far apart enough (about a few times the apparent particle diameter) from other particles and aggregates so as to disregard dipolar interactions (see Figure S3, Supporting Information).

MFM measurements were carried out at room temperature using a variable field MFM set-up from Nanotec Electrónica.[39] All the experiments were done using the lift mode (lift height: 40 nm), in which the topographic profile is retraced at a tip-sample distance where magnetostatic interactions become dominant. MFM data arise from the change in the resonance frequency of the oscillating cantilever induced by such magnetostatic coupling between tip and sample; in all the experiments shown, a phase-locked loop (PLL) was used to keep a constant phase lag between the driving signal and the cantilever oscillation, so that MFM data have units of Hz. BudgetSensors Multi75-G tips, with nominal values of spring constant k≈3N/m and resonance frequency f_0≈75 kHz, were used.

Conclusions

Summarizing, this work provides experimental characterization by variable field–magnetic force microscopy of the domain configurations in cubic, isolated $Fe_{3-x}O_4$ NPs with an average lateral size of 25-30 nm and high crystal quality. Single domain structures are reported, whose orientation and polarity are determined by both their magnetocrystalline easy axes and previous magnetic history. As the main result, we have been able to directly observe the orientation of the easy axes in individual ferrimagnetic nanoparticles. Furthermore, experimental evidence of a magnetization reversal mediated by coherent rotation of the particle spins has been obtained in these isolated NPs. These results have also been supported by micromagnetic simulations.

Acknowledgements

This work was supported by Spanish MINECO (MAT2012-33037, CSD2010-00024 and MAT2013-48054-C2) and Catalan DURSI (2009SGR856, 2014SGR220).

Notes and references

[a] Departament de Física Fonamental, Institut de Nanociència i Nanotecnologia, Universitat de Barcelona, Barcelona, 08028, Spain
[b] Instituto de Ciencia de Materiales de Madrid (ICMM-CSIC), Cantoblanco, Madrid, 28049 Spain

[c] Department of Physics, McGill University, Montreal, H3A 2T8, Canada
*Corresponding author E-mail: cmoya@ffn.ub.es
‡ These two authors contributed equally.

† Electronic Supplementary Information (ESI) available: PDF material contains TEM images of 27 nm $Fe_{3-x}O_4$ NPs (Figure S1), Thermogravimetric curve for the 27 nm $Fe_{3-x}O_4$ NPs (Figure S2) and the topography of a scan size of 20 x 20 μm of a sample (Figure S3).

1 Zeng, H.; Li, J.; Liu, J. P.; Wang, Z. L.; Sun, S. *Nature*, 2002, **420**, 395; Sun, S.; Murray, C. B.; Weller, D.; Folks, L.; Moser, A. Science, 2000, **287,** 1989.
2 Schätz, A.; Reiser, O.; Stark, W. J. *Chemistry – A European Journal*, 2010, **16**, 8950.
3 Zhang, W. *Journal of Nanoparticle Research*, 2003, **5**, 323.
4 Pankhurst, Q. A.; Connolly, J.; Jones, S. K.; Dobson, J. *Journal of Physics D: Applied Physics*, 2003, **36**, R167.
5 Perez, J. M.; Josephson, L.; Weissleder, R. *ChemBioChem*, 2004, **5**, 261.
6 Mejías, R.; Pérez-Yagüe, S.; Roca, A. G.; Pérez, N.; Villanueva, A.; Cañete, M.; Mañes, S.; Ruiz-Cabello, J.; Benito, M.; Labarta, A.; Batlle, X.; Veintemillas-Verdaguer, S.; Morales, M. P.; Barber, D. F.; Serna, C. J. *Nanomedicine*, 2010, **5,** 397.
7 Sun, C.; Lee, J. S. H.; Zhanga, M. *Advanced Drug Delivery Reviews* 2008, **60**, 1252.
8 Guardia, P.; Pérez, N.; Labarta, A.; Batlle, X. *Langmuir*, 2009, **26**, 5843.
9 Tartaj, P.; Morales M. P.; Veintemillas-Verdaguer, S.; González-Carreño, T.; Serna, C. *J. Journal of Physics D: Applied* Physics, 2003, **36**, R182.
10 Batlle, X.; Labarta, A. *Journal of Physics D: Applied Physics*, 2002, **35**, R15.
11 Salafranca, J.; Gazquez, J.; Pérez, N.; Labarta, A.; Pantelides, S. T.; Pennycook, S. J.; Batlle, X.; Varela, M. *Nano Letters*, 2012, **12**, 2499.
12 Balan, A.; Derlet, P. M., Fraile Rodríguez, A. Bansmann, J.; Yanes, R.; Nowak, U.; Kleibert, A.; Nolting, F. *Physical Review Letters* 2014, **112**, 107201.
13 Martin, Y.; Wickramasinghe, H. K. *Applied Physics Letters*, 1987, **50,** 1455.
14 Sáenz, J. J. ; García, N. ; Grütter, P. ; Meyer, E. ; Heinzelmann, H. ; Wiesendanger, R. ; Rosenthaler, L. ; Hidber, H. R. ; Güntherodt, H.-J. *Journal of Applied Physics*, 1987, **62**, 4293.
15 Jaafar, M.; Gómez-Herrero, J.; Gil, A.; Ares, P.; Vázquez, M.; Asenjo, A. *Ultramicroscopy*, 2009, **109**, 693.
16 Ivanov, Yu. P.; Iglesias-Freire, O.; Pustovalov, E. V.; Chubykalo-Fesenko, O.; Asenjo, A. *Physical Review B*, 2013, **87**, 184410.
17 Raşa, M.; Kuipers, B. W. M.; Philipse, A. P. *Journal of Colloid and Interface Science*, 2002, **250**, 303.
18 Huang, X.; Bronstein, L. M.; Retrum, J.; Dufort, C.; Tsvetkova, I.; Aniagyei, S.; Stein, B.; Stucky, G.; McKenna, B.; Remmes, N.; Baxter, D.; Kao, C. C.; Dragnea, B. *Nano Letters*, 2007, **7**, 2407.
19 Schreiber, S.; Savla, M.; Pelekhov, D. V.; Iscru, D. F.; Selcu, C.; Hammel, P. C.; Agarwal, G. *Small*, 2008, **4**, 270.
20 Dietz, C.; Herruzo, E. T.; Lozano, J. R.; Garcia, R. *Nanotechnology*, 2011, **22**, 125708.
21 Li, X; Li, Z; Pang, D; Yoshimura, S; Saito, H. *Applied Physics Letters*, 2014, **104**, 213106.
22 Sievers, S; Braun, K; Eberbeck, D; Gustafsson, S; Olsson, E; Schumacher, H.W.; Siegner, U. *Small*. 2012, **8**, 2675.
23 Block, S; Glöck, G; Weitschies, W; Helm, C.A. *Nano Letters*, 2011, **11**, 3587.
24 Wei, J. D.; Knittel, I. ; Lang, C.; Schüler, D.; Hartmann, U. *J. Nanopart. Res.*, 2011, **13**, 3345.
25 Nurgazizov, N. I. ; Khanipov, T. F.; Bizyaev, D. A. ; Bukharaev, A. A. ; Chuklanov, A. P. *Phys. Solid State*, 2014, **56**, 1817.
26 Xiaobin, Z; Grütter; P. *Physical Review B*, 2002, **66**, 024423.
27 Guardia, P; Labarta A, Batlle, X. *J. Phys. Chem.* C, 2011, **115**, 390.
28 Guardia, P; Batlle-Brugal, B; Roca, A.G.; Iglesias O.; Morales, M.P.; Serna, C. J.; Labarta, A.; Batlle, X. *J. Magn. Magn. Mater*., 2007, **316**, e756.
29 Cullity, B. D. *Introduction to Magnetism and Magnetic Materials*; Addison-Wesley: MA, 1972.
30 Heider, F.; Zitzelsberger,A.; Fabian, K. *Physics of the Earth and Planetary* Interiors, 1996, **93**, 239.
31 Zabaleta, J.; Jaafar, M.; Abellán, P.; Montón, C.; Iglesias-Freire, O.; Sandiumenge, F.; Ramos, C. A.; Zysler, R. D.; Puig, T.; Asenjo, A.; Mestres, N.; Obradors, X. *Journal of Applied Physics*, 2012, **111**, 024307.
32 Grütter, P.; Liu, Y.; LeBlanc, P.; Dürig, U. *Applied Physics Letters* 1997, **71**, 279.
33 Iglesias-Freire, Ó.; Bates, J. R.; Miyahara, Y.; Asenjo, A.; Grütter, P. H. *Applied Physics Letters*, 2013, **102**, 022417.
34 Schwarz, A.; Wiesendanger, R. *Nanotoday*, 2008, **3**, 28..
35 Neves, C. S.; Quaresma, P.; Baptista, P. V.; Carvalho, P. A.; Araujo, J. P.; Pereira, E.; Eaton, P. *Nanotechnology* 2010, **21**, 305706.
36 Jaafar, M.; Iglesias-Freire, O.; Serrano-Ramón, L.; Ibarra, M. R.; de Teresa, J. M.; Asenjo, A. *Beilstein Journal of Nanotechnology*, 2011, **2**, 552.
37 Donahue, M. J.; Porter, D. G. Interagency Report NISTIR 6376, N.I.S.T., Gaithersburg, 1999.
38 Wu, H.-C.; Arora, S. K.;Mryasov, O. N.; Shvets, I. V. *Applied Physics Letters* 2008, **92**, 182502.
39 http://www.nanotec.es.